Highlights

1. An MR thermometry is first applied to hydrate phase transition in porous medium.
2. THF hydrate growth characteristic and temperature anomaly are in-situ observed.
3. MRI signal differs significantly in space and time with the heat transfer.

An in-situ MRI method for quantifying temperature change of hydrate growth in a porous medium

Lunxiang Zhang[a], Mingrui Sun[a], Lei Yang[a], Xiaotong Zhang[b,*], Jiafei Zhao[a,*], Yongchen Song[a]

[a] *Key Laboratory of Ocean Energy Utilization and Energy Conservation of Ministry of Education, School of Energy and Power Engineering, Dalian University of Technology, Dalian 116024, P. R. China*

[b] *Interdisciplinary Institute of Neuroscience and Technology, Zhejiang University, Hangzhou 310029, P. R. China*

[*]Corresponding author. E-mail address: Xiaotong Zhang (zhangxiaotong@zju.edu.cn); Jiafei Zhao (jfzhao@dlut.edu.cn).

ABSTRACT:

The intricacy of the thermo-hydro-chemically coupled process of hydrate phase transition requires real-time in-situ observations, therefore, thermometry maps are of particular value to reveal the heat transfer process during crystal growth and dissociation. By using the temperature dependence of water proton chemical shift, the temporally- and spatially-resolved thermometry of tetrahydrofuran hydrate growths is presented in this study. Images of temperature changes were synchronously obtained by a 9.4 T ^{1}H Magnetic Resonance Imaging (MRI) system, in order to predict the saturation of aqueous solution, solid hydrate phases, and the positive temperature anomaly of exothermic reaction. Variations of MRI signal decrease and histories of temperature rise differ significantly in space and time, which have a great use for analyzing the physical micro-mechanism and the heat transfer process of hydrate growth. The

extension of these predicted results could have important implications for optimizing the phase transition process of gas hydrates.

Topical heating: Thermodynamics and Molecular-Scale Phenomena

Keywords: Hydrate phase transition; Heat transfer; Porous medium; Temperature mapping; Magnetic Resonance Imaging thermometry.

Graphical Abstract

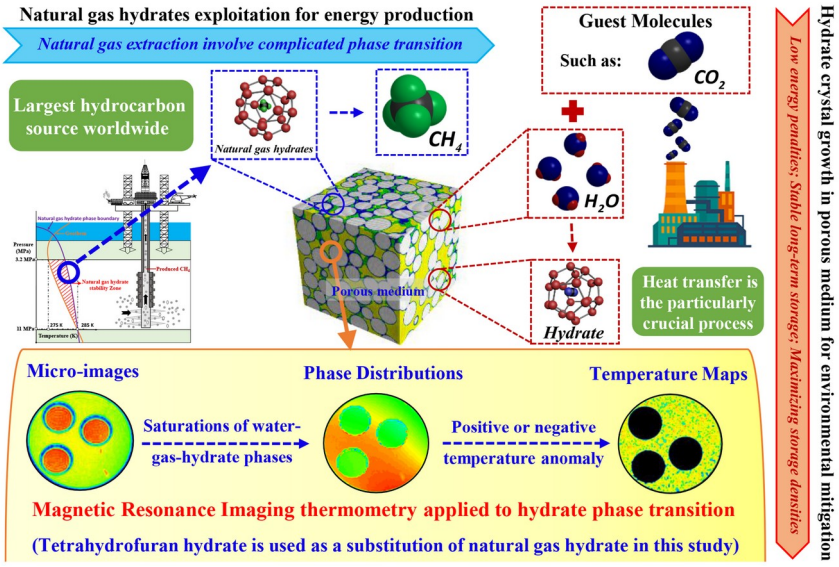

1. Introduction

Natural gas hydrates are crystalline solid compounds formed when natural gas and water coexist in environments with sufficiently low temperature and high pressure [1]. Natural gas hydrates contain enormous energy reserves and they are reported as the largest hydrocarbon source worldwide [2]. The formation of natural gas hydrates in nature and their exploitation for natural gas extraction involve complicated phase transitions, coupled with heat transfer, mass transport and diffusion, multiphase flow, as well as surface reaction kinetics [3]. Current methods to exploit natural gas hydrate accumulations are

based on breaking the thermodynamic equilibrium using temperature shifts [4], pressure variations [5], and/or chemical environment changes [6]. Up to date, these methods are still far from being cost-effective [7], in part due to unresolved and insufficient heat transfer to sustain fast hydrate dissociation [8,9]. Furthermore, in recent years, the hydrate-based technology has been considered as a promising alternative to solve numerous energy and environment related issues, such as CO_2 storage for greenhouse gas control [10], H_2 separation and purification for energy storage [11], heavy metal separation for wastewater treatment [12], desalination for potable water production [13], refrigerant as suitable cold storage mediums [14], and sugar milled increasing the solids content in aqueous carbohydrate systems [15]. Extensive efforts have been dedicated to optimizing the hydrate growth rate and the efficiency of natural gas production across various scales [16-19]. In light of the fact that the intricacy of the thermo-hydro-chemically coupled process of phase transition during hydrate formation and dissociation requires real-time in-situ observations. Thus, thermometry maps are of particular value to reveal the heat transfer process, which is essential to understand the energetics of reaction dynamics during hydrate crystal growth and dissociation.

Thermocouples [20] have been used to monitor the exothermic and endothermic performance of hydrate formation and dissociation; however, distributed thermometry monitored with thermocouples could offer only a point-temperature and would possibly destroy the hydrate sample. Infrared thermal imaging [21] has been proposed as a promising thermometry camera that applied to hydrate core-based observations; yet, Infrared camera requires a transparent medium and otherwise only detects the presence of positive or negative thermal anomalies on the core liner surface. Magnetic Resonance (MR) based thermometry is a well-established technology that has been mostly applied in biological through utilizing the thermodynamic dependence of MR characteristics [22], e.g., chemical shift, specific adsorption rate, diffusion coefficient, and relaxation time. Therefore we can possibly monitor the temperature change of a hydrate specimen with improved spatial and temporal resolutions compared to

traditional thermometry methods. In the meantime, although extensive studies in recently years have been reported to effectively investigate chemical-physical properties of hydrates by using ^{1}H water Magnetic Resonance Imaging (MRI) micro-images [9,23,24] and ^{13}C methane Nuclear Magnetic Resonance (NMR) signal [25-27], which mainly focused on cage occupancies, liquid water distributions, hydrate growth habits, hydrate dissociation characteristics, and relative permeability, unfortunately, these are not suitable for local temperature change quantification during hydrate phase transition within porous medium.

Local temperature measurement in porous medium by using MR thermometry is able to effectively quantify temperature changes during crystal hydrate growth and dissociation. Also, the MR thermometry is possibly applied to measure positive thermal anomalies for estimating hydrate plugs during pipeline transportations of liquefied natural gas.. In the present study, for the first time to the best of our knowledge, we report an MR-based thermometry method that has been applied to hydrate growth in a porous medium. A 9.4 T ^{1}H MRI system was used for imaging, alongside with tetrahydrofuran (THF) hydrate consisting of glass beads of uniform size mimicking porous medium. During the process of THF hydrate formation, varied saturations of THF-aqueous solution and solid hydrate phases were monitored, while local temperature changes were quantified with high spatiotemporal resolutions.

2. Experimental section

2.1. Materials

Quartz glass beads (ASONE, Co., Ltd., Japan) BZ-02 (0.180–0.220 mm, mean particle size $\overline{D}$ = 0.2 mm and specific gravity G_s = 1.5), tetrahydrofuran (THF, 99.0% purity, Sinopharm Chemical Reagent Co., China), deionized water (resistivity ρ = 18.2 MΩ·cm at 25 °C, supplied with a laboratory

water purification system, Aquapro2S, Aquapro International Company LLC, USA), and mineral oil (99.5% purity, Ponsure Biotechnology Co., Ltd., China)were used without further purification.

2.2. Apparatus

All experiments were conducted on a 9.4 T vertical-bore MRI system (Varian, Inc., Palo Alto, CA. US) with a 400 MHz ^{1}H millipede vertical micro-imaging probe and a maximum gradient magnetic strength of 50 Gauss/cm. In order to control experimental temperature, a refrigerated circulator (ranging from -35 to 200 °C with an estimated precision of ±0.01 °C, F25-ME, JULABO Inc., Germany) was filled with coolants (3M Fluorinert FC-40, St. Paul, MN, US), which doesn't produce MR signal and thus were not visualized in MR images. More information regarding the experimental apparatus can be found in a previous study [9].

2.3. Procedures

To evaluate the accuracy and stability of the MR-based proton resonance frequency thermometry employed in this study, two proving experiments were investigated on the specimen: (I) heating pure deionized water from 20 to 23 °C, and (II) packing the mixture of porous medium and deionized water into the MRI chamber and then heating the chamber from 0 to 10 °C gradually. Coolant FC-40 within a jacket surrounding the high-pressure chamber was used to control the heating process.

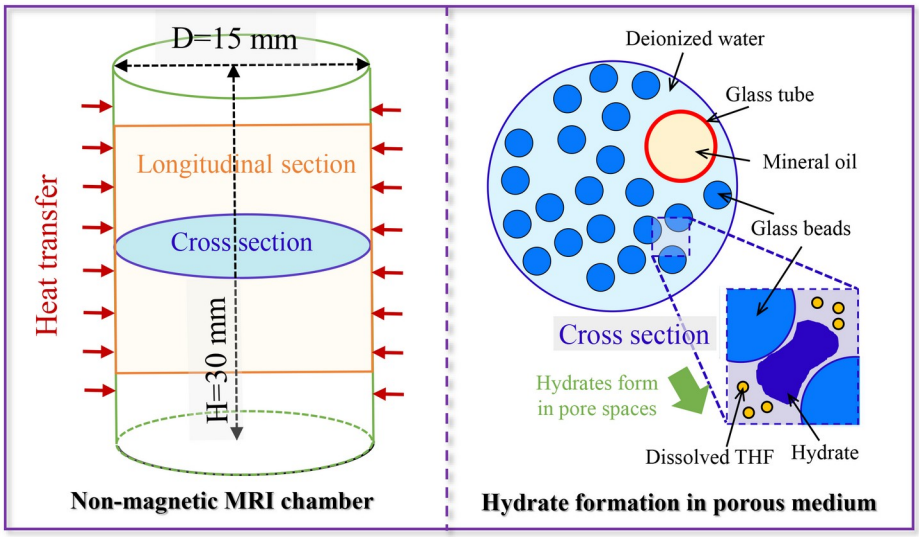

Fig. 1. Schematic diagram of non-magnetic MRI chamber and THF hydrate formation in porous medium.

THF hydrate has been widely used as a substitution of natural gas hydrate for geomechanical and geophysical investigations [28,29], although the THF is distinct from the methane in terms of the molecular size, the polarizability, and other characteristics [28]. In this study, the formation of THF hydrate was imitated by premixed aqueous solution with mass fractions of 20% THF and 80% water at 2 °C and 1 bar, which could fill 100% pore spaces in the porous medium [28]. As shown in Fig. 1, a non-magnetic (polyamide) chamber (inner diameter D_{cha} = 15 mm, height H_{cha} = 30 mm, and inside volume V_{cha} = 5.30 ml) was used to hold the specimen. Quartz glass beads BZ-02 were used to form the porous medium and to host hydrate. Three cylindrical tubes (inner diameter D_{pha} = 4.60 mm and height H_{pha} = 18 mm) filled with mineral oil provided a reference for phase drift calibration [22].

3. Thermometry principle

3.1. Proton resonance frequency thermometry

In the present study, the technique of MR-based thermometry [30] was employed in real-time temperature change (Δt) quantification over the porous medium. Up to now, the most prominent MRI thermometry methods are based on physical quantities of, i.e., the proton resonance frequency PRF, the apparent diffusion coefficient D, and the longitudinal relaxation time T_1, and the transverse relaxation time T_2, all of which have been proven to show temperature dependence measurable by MRI. However, the diffusion coefficient-, the longitudinal relaxation time- and the transverse relaxation time-based methods are relatively more time-consuming [31-37], thus unsuitable for the present study; whereas the employed proton resonance frequency method, on the contrary, has been the preferred choice for many applications [31,38,39], and thus was adopted in the present study.

The proton resonance frequency method is based on the fact that the hydrogen bonds in water are constantly strained, bent and broken by thermal fluctuations; the change in number and quality of hydrogen bonds is the main reason for the temperature dependent proton chemical shift in water that is basic to this work. The proton chemical shift causes MR image phase change by using certain types of MRI sequences (such as gradient-recalled echo GRE), and through measuring such phase change maps at different time points, we can retrieve local temperature change profiles ΔT_{PRF} at each imaging voxel through Equation (1):

$$\Delta T_{\mathrm{PRF}} = [\theta(T^{i}_{\mathrm{PRF}}) - \theta(T^{0}_{\mathrm{PRF}})]/(\alpha\gamma\tau \mathrm{B}_{0}) \tag{1}$$

where α is the temperature dependent coefficient of the pure water proton chemical shift, with a constant value of -0.01 ppm/°C in the temperature range from -20 to 100 °C [40]; γ is the gyromagnetic ratio, 2.68×10^{8} rads/sec/Tesla; τ is the echo time of applied MRI pulse sequences for encoding the field distribution as the image phase value; B_0 is the local magnetic field distribution (9.4 T in this study); $\theta(T^{0}_{\mathrm{PRF}})$ and $\theta(T^{i}_{\mathrm{PRF}})$ are the image phase values of the reference (at the starting time point) and at the i^{th} minute, respectively.

The monitored ΔT_{PRF} of all imaging voxels can be counted as the averaged proton resonance frequency thermometry result $\overline{\Delta T_{\mathrm{PRF}}}$, which could be used to define the mean relative error φ_{MR} and the standard deviation SD by using Equations (2) and (3):

$$\varphi_{\mathrm{MR}} = \frac{\left(\overline{\Delta T_{\mathrm{PRF}}} - \Delta T_{\mathrm{given}}\right)}{\Delta T_{\mathrm{given}}} \times 100\% \tag{2}$$

$$\mathrm{SD} = \sqrt{\frac{\sum_{i=1}^{n}\left(\Delta T^{i}_{\mathrm{PRF}} - \overline{\Delta T_{\mathrm{PRF}}}\right)}{n-1}} \tag{3}$$

where n is the number of imaging voxels; and ΔT_{PRF}^{i} is the proton resonance frequency thermometry result at the i^{th} pixel.

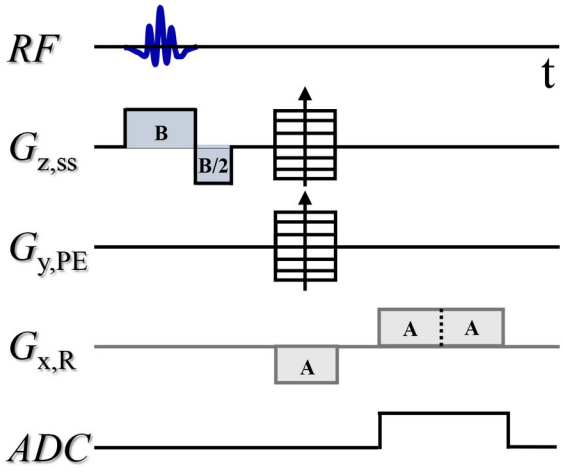

Fig. 2. Diagram of applied 3D gradient-recalled echo pulse sequence

As shown in Fig. 2, a 3D gradient-recalled echo pulse sequence for phase mapping is applied for phase mapping during hydrate phase transitions. And imaging parameters are concluded as following: time of repetition = 8.00 ms, time of echo = 1.16 ms, flip angle = 15 degree, field of view = 19.2 × 19.2 × 64 mm^3, matrix size = 96 × 96 × 32, voxel size = 0.2 × 0.2 × 2 mm^3, averages = 2, and acquisition time = 49.2 s.

3.2. Time-dependent phase saturations

The gradient-recalled echo sequence employed in this study can simultaneously obtain magnitude images of ^1H density in THF-aqueous solution during THF hydrate formation. For these images, it has been reported that the mean intensity of MR signals is proportional to the saturation of THF-aqueous solution in Equation (4). Thus, the saturation of solid THF hydrate can be described via Equation (5).

$$S_i^{sol} = \frac{I_i}{I_0} \times 100\% \tag{4}$$

$$S_i^{hyd} = \frac{(I_0 - I_i)}{I_0} \times 100\% \quad (5)$$

where I_0 and I_i are the mean intensity for THF-aqueous solution initially and at the i^{th} seconds, respectively; S_i^{sol} and S_i^{hyd} are the time-dependent phase saturation of THF-aqueous solution and solid THF hydrate.

4. Results and discussion

4.1. Heating pure deionized water

Fig. 3 summarizes the proton resonance frequency thermometry results of the experiment (I) in pure deionized water heated. The specimen filled with pure water was firstly controlled at 20 °C in the beginning, with magnitude and phase obtained by the gradient-recalled echo sequence (phase images shown in Fig. 3a). Then, the specimen was heated to 23 °C by using the refrigerated circulator, with the outlet temperature of the coolant surrounding the MRI chamber monitored by a thermocouple (Yamari Industries, Japan, ranging from -28 °C to 200 °C at a precision of ±0.1 °C); at the time of one hour after the outlet temperature was stabilized, the specimen was considered of having reached thermal equilibrium, and the magnitude and phase distribution are scanned (phase images shown in Fig. 3b). Then proton resonance frequency thermometry results ΔT_{PRF} in cross and longitudinal sections were calculated and are shown in Fig. 3c with an average temperature increase of ~3 °C ($\overline{\Delta T_{PRF}}$=3.05 in cross section and $\overline{\Delta T_{PRF}}$=2.91 in longitudinal section), implying that it's feasible to apply MR-based proton resonance frequency thermometry in accurate quantification of temperature change for water in porous medium.

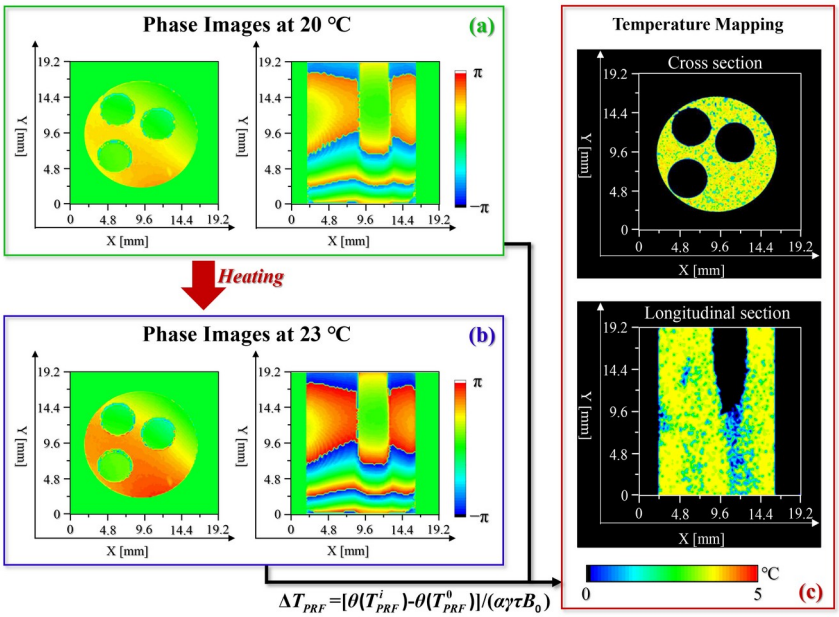

Fig. 3. MR-based proton resonance frequency thermometry results of experiment (I). (a) phase images at 20 °C; (b) phase images at 23 °C; (c) temperature mappings of ΔT_{PRF}

4.2. Heating the mixture of porous medium and deionized water

In the experiment (II), the mixed specimen of porous medium and deionized water was stepwise heated form 0 °C to 1, 3, 5, 7, and 10 °C (the black dash line and circles in Fig. 4). The magnitude image in Fig. 4 represents the liquid distribution in the cross section of the specimen. The mean intensity obtained by MRI signal in oil phase was higher than water phase because of the high ^{1}H proton density in miner oil. For the water phase, mean intensities near the walls of MRI chamber and cylindrical tubes were stronger than other parts, which could be explained by the "wall effect" (i.e., more liquid water remained near the wall where the porosity was larger than in other spaces) [41]. At each temperature step, a relatively cross proton resonance frequency temperature mapping was obtained. ΔT_{PRF} distributions in the map were almost identical and stabilized as the given temperature difference (ΔT_{given} =1, 3, 5, 7, and 10 °C), although a few abnormal pixels were observed.

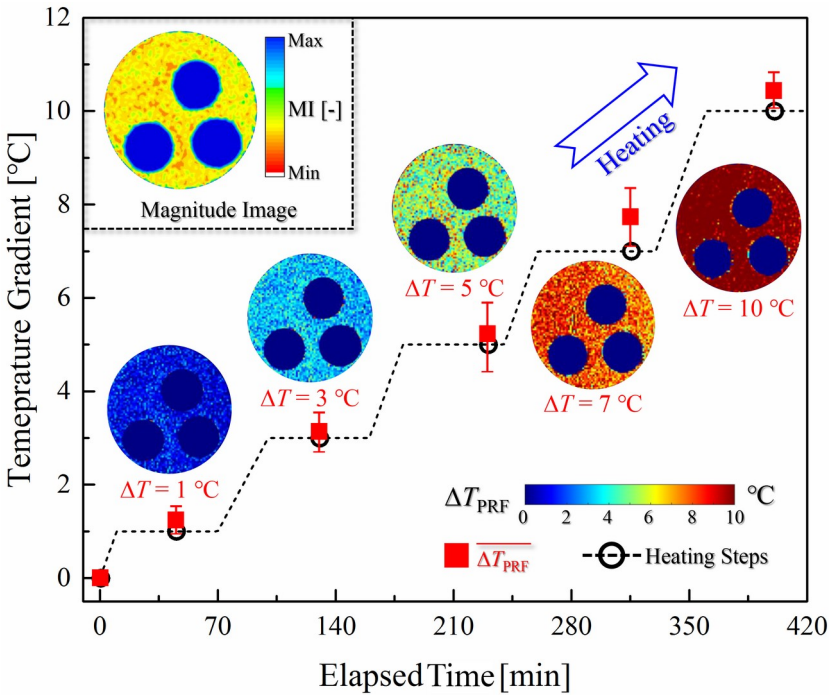

Fig. 4. MR-based proton resonance frequency thermometry results of experiment (II)

As shown in Fig. 4, $\overline{\Delta T_{PRF}}$ (red squares) exhibits a highly consistent value with each ΔT_{given} and φ_{MR} of +7.47±6.05%. Within the five ΔT_{given} of 1, 3, 5, 7, and 10 °C, standard deviations (error bars) were 0.18, 0.23, 0.76, 0.68, and 0.44, respectively. These minute variations were mainly attributed to lower signal-to-noise ratio (SNR) and sensitivity in MR phase imaging accompanied our attempts in pursuing higher spatiotemporal resolutions. To be specific, the in-plane resolution was pushed to 0.2 mm, which inevitably lowered the imaging SNR with such a small voxel size (0.08 m^3). Moreover, the cost of pushing temporal resolution to 49.2 s was a heavily "squeezed" echo time, which was adverse to a sensitive local temperature change "sniffing". It is because the local temperature change was proportional to local phase change, and the local phase change accumulated through the time duration of echo time.

4.3. THF hydrate formation

In the magnitude images during the THF formation (Fig. 5a), the red area represents miner oil, and the yellow-green area represents THF solution, and the dark-blue area represents other parts (such as, porous medium, THF hydrates, and coolants). With decreased THF solution in yellow-green areas, the random nature of the nucleation and stochastic growth of THF hydrate crystal was observable in the increased dark areas. However, THF hydrates preferred to start growing around the wall of MRI chamber and then spread to the whole specimen due to efficient heat transfer.

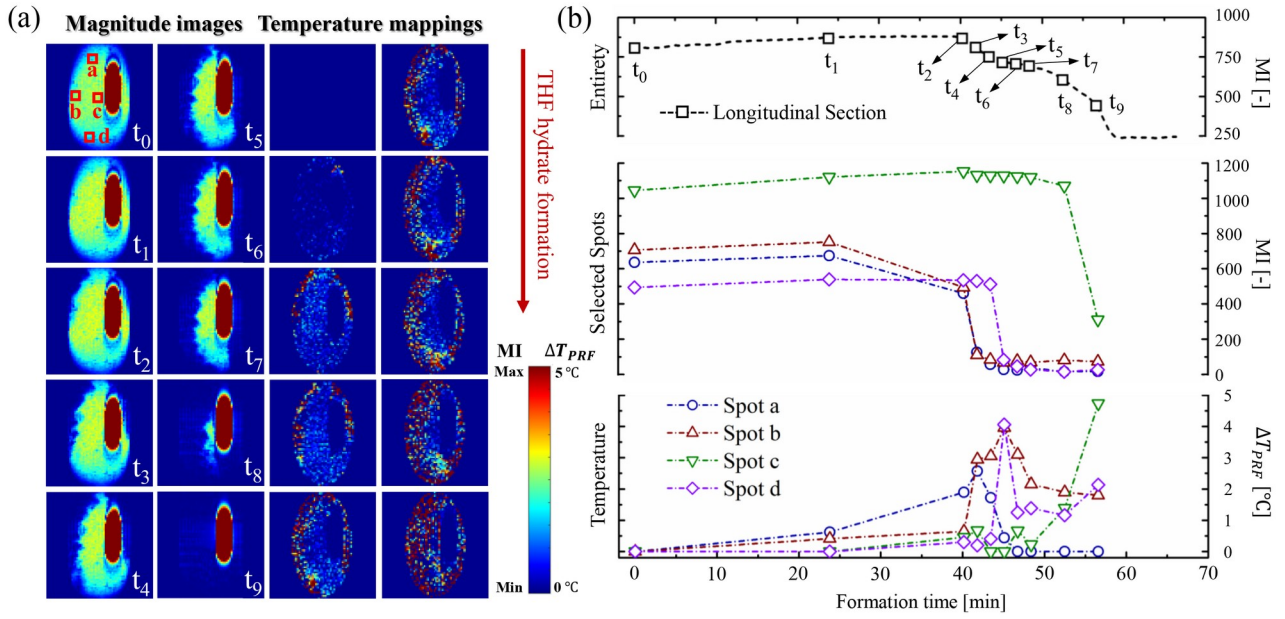

Fig. 5. Variations of mean intensities and ΔT_{PRF} during THF formation. (a) magnitude images and relative temperature mappings; and (b) formation time-resolved of mean intensities and temperature differences at the longitudinal section and four local spots.

As shown in the relative temperature maps of each magnitude images (Fig. 5a), temperature rises were observed in the region of THF hydrate formation. As this formation was an exothermic reaction, the specimen containing THF hydrate was heated relative to the ambient condition, thus creating a positive temperature anomaly. Finally, although most THF-aqueous solution was converted to solid hydrate in magnitude images (t_9), temperature changes were still sensitive to the proton resonance frequency in relative phase distributions and could be predicted with Eq. (1). Since the solid THF

hydrate also contained water molecules (hydrogen atoms), it also produced MRI signal, thus we were still able to obtain MR magnitude and phase images. However, the transverse relaxation time T_2 of frozen water (solid hydrate herein) decreased significantly compared to its liquid state [42], therefore it was anticipated that using the same echo time would inevitably produce weaker MRI signal intensity, leading to lower SNR in magnitude images.

To assess the spatial and temporal resolution of proton resonance frequency thermometry applied in THF hydrate formation, four voxels on the magnitude image were randomly selected. Fig. 5b summarizes the mean intensity variations and relative temperature change histories of the four selected spots. The time-dependent phase saturation of THF-aqueous solution S_1^{sol} and solid THF hydrate S_1^{hyd} could be quantified using the mean intensity of the MRI data by Eqs. (4) and (5). In spots b, c, and d, the mean intensity was less than it was in the entire specimen, whereas in spot a it was higher than the mean intensities history curve of the THF hydrate sample. Simultaneously, the temperature change of the four spots ($0.2\times0.2\times2$ mm^3) crossed through THF hydrate formation that differed significantly in space and time. These results demonstrated that mean intensities and ΔT_{PRF} obtained by phase mapping pulse sequence in MRI have a great use for analyzing the physical mechanism of hydrate growth.

4.4. Temporal and spatial resolutions

In the present study, the temporal resolution was limited to ~49 sec for phase/temperature "snapshot". Nevertheless, the temporal resolution can be further improved by using state-of-the-art fast MRI methods such as simultaneous multi-slice excitation [42,43], parallel imaging in data acquisition [44], and phased array in receive coil design [45] etc. Moreover, the spatial resolution of 0.2 mm can be further improved with stronger gradient systems and/or at higher main magnetic field strengths [46].

4.5. Application of the proton resonance frequency thermometry in porous medium

There have been only few studies of MRI thermometry applying MR-based thermometry to chemical conversion processes in porous medium involving heat transfer and mass transport. A 1D ^{27}Al MRI thermometry technique was reported to monitor the signal intensity of the Pd/γ-Al_2O_3 catalyst in an operating catalytic reactor, and the results suggested a pronounced temperature dependence of MRI signal intensity, which could help to convert into the quantitative values of local temperature [47]. However, such conversion is limited by lacking of feasible calibration method and has insufficient sensitivity to 2D and 3D local temperature mappings. A gas-phase-enriched ^{1}H NMR thermometry technology was proposed to measure a non-invasively gas temperature mapping during propylene and hydrogen reacted to form propane in metal nanoparticles and metal-organic framework catalysts, within the measure errors of 4% of the local temperature [46], this motional-averaging NMR method created a applicably temporal resolution (~30 min) that outperformed existing thermometry techniques (~2.5 h) with a reasonable precision, but it still could not meet the time precision that a rapid physicochemical process requires. In the present study, the employed proton resonance frequency thermometry technique has significant advantages in 3D real-time temperature change quantification with higher spatiotemporal resolutions and it has been successfully applied into porous medium. We expect this technique would be applicable to most industrially relevant reaction in porous medium, including porous plate heat exchanger, aero-dynamic heat-resistant porous coating, cold storage in porous materials, and artificial ground freezing, etc.

4.6. Secondary hydrate formation and pore plugging

Secondary hydrate formation and ice generation remain as a major challenge in natural gas hydrate exploitation, which would plug the pores with low permeability and have a detrimental impact for a sustainable natural gas production [48]. Extensive efforts in laboratory-scale investigations and reservoir-scale simulations demonstrated that secondary hydrate formation during dissociation could be caused by Joule-Thomson effect [49] and local repressurization [50], yet without sufficient microscale

evidence. Our preliminary efforts reported in this study attempts to predict the positive thermal abnormal of secondary hydrate formation, for the purpose of preventing the pore plugging during natural gas hydrate exploitation, and managing the natural gas recovery way for the optimizing production rate.

5. Conclusions

Despite the need for further investigation and improvement, in this study, water proton chemical shift has proven to be a successfully temporal-spatial resolution thermometry method for phase transitions of hydrate crystals in porous medium. The THF hydrate growth characteristic and positive temperature anomaly synchronously observed herein can provide the heat generated information and physicochemical property of hydrate formation. Our experimental results have important implications for optimizing the growth rate of hydrate crystal and the exploitation efficiency of natural gas.

CRediT authorship contribution statement

Lunxiang Zhang: Conceptualization, Investigation, Writing-original draft, Funding acquisition; **Mingrui Sun:** Investigation, Data curation; **Lei Yang:** Funding acquisition, Validation; **Xiaotong Zhang:** Methodology, Investigation, Funding acquisition, Writing-review & editing; **Jiafei Zhao:** Supervision, Resources, Writing-original draft; **Yongchen Song :** Supervision, Funding acquisition.

Declaration of Competing Interest

The authors declared that there is no conflict of interest.

Acknowledgement

This work was supported by the National Natural Science Foundation of China (Grant No. 52006024, 51806027, 81701774, 61771423) and the Major Program of National Natural Science Foundation of China (Grant No. 51436003).

References

[1] Sloan ED. Fundamental principles and applications of natural gas hydrates. Nature 2003;426(6964):353-359.

[2] Milkov AV. Global estimates of hydrate-bound gas in marine sediments: how much is really out there. Earth-Sci Rev 2004;66(3-4):83-197.

[3] Sloan ED, Koh KC. Clathrate hydrates of natural gases. third ed., Boca Raton: CRC Press, 2008.

[4] Song YC, Wang JQ, Liu Y, Zhao JF. Analysis of heat transfer influences on gas production from methane hydrates using a combined method. Int J Heat Mass Transf 2016;92:766-773.

[5] Wan QC, Si H, Li B, Li G. Heat transfer analysis of methane hydrate dissociation by depressurization and thermal stimulation. Int J Heat Mass Transf 2018;127:206-217.

[6] Shagapov VS, Khasanov MK, Musakaev NG, Duong NH. Theoretical research of the gas hydrate deposits development using the injection of carbon dioxide. Int J Heat Mass Transf 2017;107:347-357.

[7] Makogon YF, Holditch SA, Makogon TY. Natural gas-hydrates-a potential energy source for the 21st century. J Petrol Sci Eng 2007;56(1-3):14-31.

[8] Circone S, Stern LA, Kirby SH. The role of water in gas hydrate dissociation. J Phys Chem B 2004;108(18):5747-5755.

[9] Zhang LX, Zhao JF, Dong HS, Zhao YC, Liu Y, Zhang Y, Song YC. Magnetic resonance imaging for in-situ observation of the effect of depressurizing range and rate on methane hydrate dissociation. Chem Eng Sci 2016;144:135-143.

[10] Zhang LX, Yang L, Wang JQ, Zhao JF, Dong HS, Yang MJ, Liu Y, Song YC. Enhanced CH_4 recovery and CO_2 storage via thermal stimulation in the CH_4/CO_2 replacmemnt of methane hydrate. Chem Eng J 2017;308:40-49.

[11] Lokshin KA, Zhao YS. Fast synthesis method and phase diagram of hydrogen clathrate hydrate. Appl Phys Lett 2006;88(13):131909.

[12] Dong HS, Zhang LX, Ling Z, Zhao JF, Song YC. The controlling factors and ion exclusion mechanism of hydrate-based pollutant removel. ACS Sustain Chem Eng 2019;7(8):7932-7940.

[13] Han S, Shin JY, Rhee YW, Kang SP. Enhanced efficiency of salt removal from brine for cyclopentane hydrates by washing, centrifuging, and sewating. Desalination 2014;354:17-22.

[14] Cheng CX, Wang F, Tian YJ, Wu XH, Zheng JL, Zhang J, Li LW, Yang PL, Zhao JF. Review and prospects of hydrate cold storage technology. Renew Sust Energ Rev 2020;117:109492.

[15] Smith A, Babaee S, Mohammadi AH, Naidoo P, Ramjugernath D. Clathrate hydrate dissociation conditions for refrigerant+ sucrose aqueous solution: experimental measurement and thermodynamic modeling. Fluid Phase Equilibria 2016;413:99-109.

[16] Kvenvolden KA. Gas hydrates-geological perspective and global change. Rev Geophys 1993;31(2):173-187.

[17] Kwon TH, Cho GC, Santamarina JC. Gas hydrate dissociation in sediments: pressure-temperature evolution. Geochem Geophy Geosy 2008;9(3).

[18] Lei L, Santamarina JC. Laboratory strategies for hydrate formation in fine-grained sediments. J. Geophys Res-Sol Ea 2018;123(4):2583-2596.

[19] Ghaani MR, English NJ. Molecular-dynamics study of propane-hydrate dissociation: fluctuation-dissipation and non-equilibrium analysis. J Chem Phys 2018;148(11):114504.

[20] Wang Y, Feng JC, Li XS, Zhang Y, Chen ZY. Fluid flow mechanisms and heat transfer characteristics of gas recovery from gas-saturated and water-saturated hydrate reservoirs. Int J Heat Mass Transf 2018;118:1115-1127.

[21] Weinberger JL, Brown KM, Long PE. Painting a picture of gas hydrate distribution with thermal images. Geophys Res Lett 2005;32(4).

[22] Zhang XT, Moortele PFV, Liu JE, Schmitter S, He B. Quantitative prediction of radio frequency induced local heating derived from measured magnetic field maps in magnetic resonance imaging: A phantom validation at 7 T. Appl Phys Lett 2014;105(24):244101.

[23] Bagherzadeh SA, Moudrakovski L, Ripmeester JA, Englezos P. Magnetic resonance imaging of gas hydrate formation in a bed of silica sand particles. Energ Fuel 2011;25(7):3803-3092.

[24] Zhang LX, Kuang YM, Dai S, Wang JQ, Zhao JF, Song YC. Kinetic enhancement of capturing and storing greenhouse gas and volatile organic compound: micro-mechanism and micro-sturcture of hydrate growth. Chem Eng J 2020;397:122357.

[25] Kuang YM, Zhang LX, Song YC, Yang L, Zhao JF. Quantitative determination of pore-structure change and permeability estimation under hydrate phyase transition by NMR. AIChE J 2019;e16859.

[26] Seo Y, Kang SP, Jang W. Structure and composition analysis of natural gas hydrates: ^{13}C NMR spectroscopic and gas uptake measurements of mixed gas hydrates. J Phys Chem A 2009;113(35):9641-9649.

[27] Gupta A, Dec SF, Koh CA, Sloan ED. NMR investigation of methane hydrate dissociation. J Phys Chem C 2007;115(5):2341-2346.

[28] Yun TS, Santamarina JC, Ruppel C. Mechanical properties of sand, silt, and clay containing tetrahydrofuran hydrate. J Geophys Res-Sol Ea 2007;112:B4.

[29] Li DL, Peng H, Liang DQ. Thermal conductivity enhancement of clathrate hydrate with nanoparticles. Int J Heat Mass Transf 2017;104:566-573.

[30] Ishihara Y, Calderon A, Watanabe H, Okamoto K, Suzuki Y, Kuroda K, Suzuki Y. A precise and fast temperature mapping using water proton chemical shift. Magn Reson Med 1995;34(6):814-823.

[31] Rieke V, Pauly KB. Echo combination to reduce proton resonance frequency (PRF) thermometry errors from fat. J Magn Reson Imaging 2008;27(3):673-677.

[32] Baron P, Ries M, Deckers R, Greef M, Tanttu J, Kohler M, Viergever MA, Moonen CYW, Bartels LW. In vivo T_2-based MR thermometry in adipose tissue layers for high-intensity focused ultrasoud near-field monitoring. Magn Reson Med 2014;72(4):1057-1064.

[33] Baron P, Deckers R, Knuttel FM, Bartels LW. T_1 and T_2 temperature dependence of female human breast adipose tissue at 1.5 T: groundwork for monitoring thermal therapies in the breast. NMR Biomed 2015;28(11):1463-1470.

[34] Gensler D, Fidler F, Ehses P, Warmuth M, Reiter T, During M, Ritter O, Ladd ME, Quick HH, Jakob PM, Bauer WR, Nordbeck P. MR safety: fast T_1 thermometry of the RF-induced heating of medical devices. Magn Reson Med 2012;68(5):1593-1599.

[35] Hynynen K, McDannold N, Mulkern RV, Jolesz FA. Temperature monitoring in fat with MRI. Magn Reson Med 2000;43(6):901-904.

[36] Kuroda K, Iwabuchi T, Obara M, Honda M, Saito K, Imai Y. Temperature dependence of relaxation times in proton components of fatty acids. Magn Reson Med Sci 2011;10(3):177-183.

[37] Todd N, Diakite M, Payne A, Parker DL. In vivo evaluation of multi-echo hybrid PRF/T_1 approach for temperature monitoring during breast MR-guided focused ultrasound surgery treatments. Magn Reson Med Sci 2014;72(3):793-799.

[38] McDannold N, Tempany C, Jolesz F, Hynynen K. Evaluation of referenceless thermometry in MRI-guided focused ultrasound surgery of uterine fibroids. J Magn Reson Imaging 2008;28(4):1026-1032.

[39] Odéen H, Almquist S, Bever J, Christensen DA, Parker DL. MR thermometry for focused ultrasound monitoring utilizing model predivtive filtering and ultrasound beam modeling. J Ther Ultrasound 2016;4(1):23.

[40] Oh S, Webb AG, Neuberger T, Park B, Collins CM. Experimental and numerical assessment of MRI-induced temperature change and SAR distributions in phantoms and in vivo. Magn Reson Med 2010;63(1):218-223.

[41] Zhang LX, Kuang YM, Zhang XT, Song YC, Liu Y, Zhao JF. Analyzing the process of gas production from methane hydrate via nitrogen injection. Ind Eng Chem Res 2017;56(26):7585-7592.

[42] Moeller S, Yacoub E, Olman CA, Auerbach E, Strupp J, Harel N, Ugurbil K. Multiband multislice GE-EPI at 7 tesla, with 16-fold acceleration using partial parallel imaging with application to high spatial and temporal whole-brain fMRI. Magn Reson Med 2010;63(5):1144-1153.

[43] Setsompop K, Gagoski BA, Polimeni JR, Witzel T, Wedeen VJ, Wald LL. Blipped-controlled aliasing in parallel imaging for simultaneous multislice echo planar imaging with reduced g-factor penalty. Magn Reson Med 2012;67(5):1210-1224.

[44] Pruessmann KP, Weiger M, Scheidegger MB, Boesiger P. SENSE: sensitivity encoding for fast MRI. Magn Reson Med 1999;42(5):952-962.

[45] Keil B, Wald LL. Massively parallel MRI detector arrays. J Magn Reson 2013;229:75-89.

[46] Jarenwattananon NN, Glöggler S, Otto T, Melkonian A, Morris W, Burt SR, Yaghi OM, Bouchard LS. Thermal maps of gases in heterogeneous reactions. Nature 2013;502(7472):537-540.

[47] Koptyug IV, Khomichev AV, Lysova AA, Sagdeev RZ. Spatially resolved NMR thermometry of an operating fixed-bed catalytic reactor. J Am Chem Soc 2008;130(32):10452-10453.

[48] Lee J, Park S, Sung W. An experimental study on the productivtity of dissociated gas from gas hydrate by depressurization scheme. Energ Convers Manage 2010;51(12):2510-2515.

[49] Seol Y, Myshakin E. Experimental and numerical observations of hydrate reformation during depressurization in core-scale reactor. Energy Fuel 2011;25(3):1099-1100.

[50] Henry P, Thomas M, Clennell MB. Formation of natural gas hydrates in marine sediments: 2. thermodynamic calculations of stability conditions in porous sediments. J Geophys Res-Sol Ea 1999;104(B10):23005-23022.